Spin-dependent quantum optics in a quantum dot molecule

Bumsu Lee, Brennan C. Pursley, Samuel G. Carter, Sophia E. Economou, Michael K. Yakes, Joel Q. Grim, Allan S. Bracker, and Daniel Gammon

Phys. Rev. B **100**, 125438 — Published 30 September 2019

DOI: 10.1103/PhysRevB.100.125438

Spin-dependent quantum optics in a quantum dot molecule

Bumsu Lee[1], Brennan C. Pursley[1], Samuel G. Carter,[2] Sophia E. Economou[3], Michael K. Yakes[2], Joel Q. Grim[2], Allan S. Bracker[2], and Daniel Gammon[2]

[1]NRC Research Associate at the Naval Research Laboratory, 4555 Overlook Ave. SW, Washington, DC 20375, USA

[2]Naval Research Laboratory, 4555 Overlook Ave. SW, Washington, DC 20375, USA

[3]Department of Physics, Virginia Tech, 850 West Campus Drive, Blacksburg, VA 24061, USA

Abstract:

A pair of tunnel-coupled quantum dots has advantages over single dots in tunability and spin coherence, but far less work has been done to measure and understand the quantum optics of this system. In particular, the two-electron singlet-triplet system with one electron in each dot generates a unique eight-level system in which two-level and four-level double Λ systems are only coupled through the hyperfine interaction and other spin relaxation processes. We first measure the emission spectrum under resonant driving with a continuous wave laser and then perform time-correlated Hanbury Brown-Twiss (HBT) and Hong-Ou-Mandel (HOM) interferometric measurements to examine non-classical photon properties of spin-flip Raman emission and resonance fluorescence. The shapes of second order correlation functions [$g^{(2)}(\tau)$] from HBT are strikingly different between resonance fluorescence and spin-flip Raman emission, reflecting the spin dynamics of the singlet-triplet system. In addition, our two-photon HOM measurements demonstrate a high raw visibility of 0.96, with a coherence time exceeding the radiative lifetime.

I. Introduction

Self-assembled InGaAs quantum dots (QDs) are an excellent source of single and entangled photons that have high indistinguishability, fast emission rates, and high single photon purity [1,2]. The quantum optics of two-level systems in QDs have been studied extensively, showing non-classical properties of light such as photon anti-bunching [3–5], two photon interference [6–8], Rabi oscillations [9] and the Mollow triplet [10–12]. Quantum dots can also host an electron or hole spin that provides a quantum memory as well as a three-level Lambda (Λ) system, which is typically formed in the charged QDs by applying a magnetic field [13,14]. This system provides better control over the temporal and spectral profile of single photon generation [8,15–18] and a quantum interface between spin qubits and photon qubits [19–24]. A quantum dot molecule (QDM), composed of two vertically stacked quantum dots separated by a thin tunnel barrier [25,26], offers additional capabilities, including energy tuning and the singlet-triplet spin system [27–29]. The doubly-charged QDM provides a Λ system formed with the ground state singlet and $M_s = 0$ triplet. This spin system does not require a high magnetic field and can be less sensitive to environmental fluctuations than a single dot system [29]. Previous work in this system has examined the bias-dependent photoluminescence [27], optical spin pumping and coherent control [28,30], Raman and resonance fluorescence [17,31,32], coherent population trapping [29,30], coupling to optical cavities [32], and spin-photon entanglement [24]. In many of these studies, simplified energy level systems were considered, and measurements of the emitted photon statistics were very limited. In particular, the connection between the quantum optical properties and the ground state spin have not been measured. This article provides a more complete look at the quantum optics of this system.

The quantum optics of an emitter can be well-characterized by measuring the first order correlation function $g^{(1)}(\tau)$, the second-order correlation function $g^{(2)}(\tau)$, and Hong-Ou-Mandel (HOM) indistinguishability. The first order (field) correlation function $g^{(1)}(\tau)$ reflects the frequency and coherence of photons and is typically measured with an interferometer. The Fourier transform of $g^{(1)}(\tau)$ is proportional to the emission spectrum of the emitter, providing equivalent information. The second order (intensity) correlation function $g^{(2)}(\tau)$ reflects the time-correlations in photon emission, and is measured with Hanbury Brown-Twiss (HBT) interferometry, in which photons are incident on a 50:50 beamsplitter sending photons to two detectors [33]. The probability of detecting a second photon after the detection of a first is measured. This measurement provides the single photon purity of the quantum light source and reflects the population dynamics of the emitter. HOM measurements are a variation of HBT interferometry, in which two photons are incident on the beamsplitter, giving rise to photon bunching when they are indistinguishable [34].

In this article, we report on the quantum optics of the singlet-triplet system of a QDM charged with two electrons, performing all three of these measurements under resonant continuous-wave (CW) laser excitation. We find that a key feature of understanding this system is that it consists of two subsystems: a double Λ system with the singlet (S) and $M_s = 0$ triplet (T_0), and a double two-level system with the $M_s = \pm 1$ triplets ($T_\pm$) [28]. These subsystems are only coupled through spin relaxation processes and give very different behavior in quantum optics. Because of the polarization selection rules of this system, we can measure the optical processes of primarily just one of these subsystems by spectrally resolving emission, either measuring resonance fluorescence (RF) [35], centered on the drive laser, or Raman spin-flip emission [17,31,32], separated from the laser by the exchange splitting. We first measure the

emission spectra of this resonantly driven system, which is consistent with a dressed state model, reaching the interesting limit where the Rabi frequency exceeds the exchange splitting [36]. Then we measure $g^{(2)}(\tau)$ for both RF and Raman emission under more modest drive conditions, which show strikingly different temporal behavior, reflecting the two different subsystems and their spin dynamics. Finally, we perform HOM measurements for both optical processes, which also have different behavior. The results are all well-described by a quantum optics model of the system that helps explain the dynamics behind the optical measurements.

II. Sample and system

Epitaxially grown InGaAs QDMs (two QDs separated by a 3/2/4 nm GaAs/AlGaAs/GaAs tunnel barrier) on an *n*-doped GaAs substrate are embedded in a vertical *n-i-n-i-p* diode structure for electron injection and within a distributed Bragg reflector (DBR) planar cavity. A zirconia hemispherical solid immersion lens (SIL) was placed on the top surface of the sample to enhance the collection efficiency. The charge state of a QDM can be deterministically controlled by applying the electrical bias via electron injection. In the two-electron (2-e) charged QDM with one electron residing in each QD, the exchange interaction energetically separates the spin singlet (S) and the three degenerate triplet (T_0, T_+, T_-) ground states, as shown in Fig. 1(a). The spin singlet has a large curvature due to the anticrossing of the singlet state with charge configurations having both electrons in one QD. The energy level diagram in Fig. 1(b) shows that there are two different subsystems: a four-level double Λ system with S and T_0 ground states, and a double two-level system with the T_+ and T_- ground states. S and T_0 ground states are both coupled to the two exciton states with orthogonal linear polarizations, forming the two overlapping Λ systems, while T_+ and T_- each couple to only one exciton state with opposite circular polarizations. Nominally, these subsystems do not connect to each other through optical processes, and moving from one to the other only occurs through spin relaxation. Spin relaxation can occur through cotunneling of electrons to the nearby *n*-doped layer and depends strongly on bias [37,38]. The two electron charge state is stable over a range of biases, and cotunneling is strongest at the edges. Spin relaxation can also occur through the hyperfine interaction, which is strongest for electron spins. Valence band mixing may also relax selection rules and give similar effects as spin relaxation.

In Fig. 1(c), the singlet (S) and triplet (T_0, T_+, T_-) transitions are measured as a function of the bias using differential reflectance (DR) [39]. The exchange splitting Δ_{exc} ranges from 50 to 125 μeV in this bias region. The DR signal is suppressed at the center of the stable bias range, due to optical spin pumping where the spin relaxation rate is longest [13,14,28]. With the laser on the S transition, optical excitation drives the system into T_0, causing the transition to go dark and suppressing the DR signal. With the laser on the T transitions, there is similar pumping, but T_+ and T_- can only be depleted by mixing of the states in the two subsystems, likely through the hyperfine interaction. The DR signal is strongest at the charge stability edge where strong spin relaxation constantly equalizes the spin states.

III. Spectrum of the strongly-driven QDM

In order to understand the optical processes of this system, we first measure the emission spectrum while resonantly driving the triplet transitions, as displayed in Fig. 2(a) for a series of drive powers.

These spectra were measured with a triple spectrometer and CCD camera with 18 μeV resolution. The spectra for this figure were obtained from a different QDM than in Fig. 1, having a larger Δ_{exc} of 190 μeV. The spin relaxation is also relatively fast in this QDM, so we do not expect any effects from optical pumping. The drive laser is polarized vertically, and only horizontally polarized light is collected in order to suppress scattered laser light. For the lowest drive power in Fig. 2(a), there is emission from two peaks – at the singlet and triplet transitions. The emission at the singlet corresponds to Raman spin flip emission that can occur when the system is in the T_0 state. The emission at the triplet corresponds to RF from the T_+ and T_- transitions. These transitions are circularly polarized, so excitation and emission with orthogonal polarizations is possible. RF from T_0 is suppressed because it has the same polarization as the laser. (Because there are two degenerate T_0 transitions with orthogonal polarizations, driving the T_0 transitions always results in a polarization aligned with the laser, resulting in no cross-polarized emission without a change in the exciton state.) This results in the interesting situation where Raman emission originates from the $S - T_0$ subsystem, and RF originates from the $T_\pm$ subsystem.

As the drive power increases, many more emission lines appear, starting with Autler-Townes splitting of the anti-Stokes Raman near the singlet transition [40] and the Mollow triplet near the triplet transition [41]. These lines can be understood using the dressed state diagram in Fig. 2(b), in which the ground and excited states of the resonantly driven transitions, $T_0 \rightarrow X_2$, $T_+ \rightarrow X_3$, and $T_- \rightarrow X_4$ are all symmetrically split by $\pm\Omega/2$. The $S \rightarrow X_1$ transition is driven off-resonance, detuned by Δ_{exc}, resulting in an asymmetric splitting by $\frac{1}{2}\Delta_{\text{exc}} \pm \frac{1}{2}\sqrt{\Omega^2 + \Delta_{\text{exc}}^2}$ for S and $-\frac{1}{2}\Delta_{\text{exc}} \pm \frac{1}{2}\sqrt{\Omega^2 + \Delta_{\text{exc}}^2}$ for X_1. For cross-polarized emission, all possible transitions between dressed states are possible for the $T_\pm$ subsystem, resulting in the Mollow triplet. For the $S - T_0$ subsystem, only diagonal transitions are detected, giving eight emission lines. Two of these correspond to the strong anti-Stokes Raman lines split by Ω, appearing near the singlet transition. Two correspond to the much weaker Stokes Raman lines split by Ω, appearing below the laser by about Δ_{exc}. The other four lines are also weak and appear close to the laser, within the sidebands of the Mollow triplet. In Fig. 2(c) the peak positions are plotted as a function of Ω along with the transition energies from a dressed state model. The agreement is excellent and shows a highly non-perturbative regime where $\Omega > \Delta_{\text{exc}}$ and there are crossings between the emission lines [36]. In Fig. 2(a) we also plot a model of the emission spectrum, obtained by numerically integrating the master equation of the driven eight-level system and calculating the Fourier transform of $g^{(1)}(\tau)$ for all allowed transitions (see Appendix) [42,43]. The agreement is quite good when convoluting the spectra with the spectrometer resolution.

IV. $g^{(2)}(\tau)$ of the driven QDM

To further understand the quantum optics of this system, we study the intensity autocorrelation function $g^{(2)}(\tau)$, which we obtain from HBT measurements on the QDM from Fig. 1. These measurements are performed at moderate drive powers, with Rabi frequencies of ~ 1.5 GHz or less, in order to resolve the temporal behavior of $g^{(2)}(\tau)$. Fig. 3(a) displays the emission spectrum for RF and Raman while resonantly driving the triplet transitions, showing the Mollow triplet and Autler-Townes doublet. High spectral resolution is obtained by sending emitted light through a scanning Fabry-Perot interferometer with 1 μeV resolution. For HBT measurements the emission is spectrally filtered around either the singlet or triplet transition using a Fabry-Perot interferometer with 10 μeV bandwidth. This

allows us to separate Raman and RF while still maintaining high temporal resolution. Raman and RF photons in our mixed Λ and two-level system have very distinct behavior for $g^{(2)}(\tau)$. Fig. 3(b) displays $g^{(2)}(\tau)$ of singlet Raman emission, with an antibunching dip near zero time delay that rises to a constant value of 1 with a time constant of 1.8 ns. High single photon purity is characterized by the low value of this antibunching dip [$g^{(2)}(0) = 0.042$], which is limited by the time resolution of the system. The rise time of the $g^{(2)}(\tau)$ function is significantly longer than the spontaneous emission time of the system (0.84 ns). The longer rise time is due to the fact that emission of the first Raman photon puts the system in the S state, after which it cannot emit another Raman photon until returning to the T_0 state through spin relaxation or other optical processes. This wait time also suppresses Rabi oscillations, which can sometimes be very weakly observed in the Raman $g^{(2)}(\tau)$.

Figure 3(c) displays $g^{(2)}(\tau)$ for the triplet RF, showing strong Rabi oscillations with an antibunching dip at zero time delay, that is shifted far above zero due to fast oscillations (1.45 GHz) measured with limited time resolution. The first photon detected projects the system into T_+ or T_-, and the probability of emitting a second photon is then proportional to the population of X_3 or X_4, giving rise to Rabi oscillations. In Fig. 3(d), the Rabi frequency is plotted vs. the square root of power, confirming the expected linear dependence. The Rabi frequency appears to approach a nonzero value at zero power, consistent with a small detuning (~0.35 GHz) of the laser from the triplet transition. There is also a clear bunching-like decay of $g^{(2)}(\tau)$ at longer times with a decay time of 2.45 ns, reminiscent of blinking behavior [44,45]. This bunching effect can be understood in terms of competition between the two subsystems. As stated previously, when the laser is resonant with the triplet transitions, optical pumping should eventually drive the system into the S state, limited by the spin relaxation rate. After detection of the first photon, the system must be in the $T_\pm$ subsystem and is likely to emit another photon. As optical pumping occurs, the system is more likely to be in the S state where no RF can be detected. The bunching decay time thus represents the time to achieve the steady state population under these conditions. In analogy with blinking, we can also consider the $S - T_0$ subsystem to play the role of a dark or hidden state with no RF.

Further insight into this behavior and the associated spin dynamics of the system can be obtained by measuring the dependence of $g^{(2)}(\tau)$ on bias. The main effect of bias here is to vary the spin relaxation rate from cotunneling, γ_{cot}. Fig. 4(a,b) shows the respective bias-dependent $g^{(2)}(\tau)$ for Raman and RF, along with a model of $g^{(2)}(\tau)$ that includes spin relaxation from cotunneling and the hyperfine interaction. Several biases were selected, going from the charge stability edge to the middle of the stability range (see Fig. 1(c) for comparison). Data was difficult to obtain at the center of the stability range, particularly for Raman data, because optical pumping reduced the emission to very low levels. For the Raman data, there is a long rise time of 5 ns at $V = 744$ mV, closest to the center of the stability range, where cotunneling should be weak. The rise time is very fast (400 ps) near the charge stability edge at $V = 732$ mV, where cotunneling is strongest. The rise time is clearly influenced by spin relaxation from cotunneling, but there are other factors that also affect the rise time. In particular, optical processes, such as the off-resonant Stokes Raman process, return the system to T_0 and allow another anti-Stokes Raman photon to be emitted without any ground state spin relaxation. These optical processes become more important when cotunneling is weak and when the drive power is higher. Higher drive powers decrease the rise time.

The RF [Fig. 4(b)] shows extreme bunching behavior at the center of the stability range at $V = 752$ mV, with $g^{(2)}(0)$ going up to 25. There are Rabi oscillations damped by optical dephasing, followed by slow decay with a time constant of 13.4 ns. As the bias moves toward the stability edge at 732 mV, the bunching effect gets weaker and occurs on shorter timescales. At $V = 732$ mV the bunching is essentially gone, and even the Rabi oscillations are heavily damped by the fast spin relaxation.

All of this behavior can be described very well by the model of the driven eight-level system. The RF is modelled with the correlation function for the $T_+ \leftrightarrow X_3$ and $T_- \leftrightarrow X_4$ transitions (which behave identically), and the Raman is modelled with the correlation function for the $S \leftrightarrow X_2$ transition. The free parameters are the Rabi frequency Ω, the radiative decay rate Γ, the cotunneling spin relaxation rate γ_{cot}, and the hyperfine spin relaxation rate γ_{hyp}. Cotunneling is assumed to give equal relaxation rates between any two spin states in the ground state or excited state. The hyperfine interaction should only lead to efficient relaxation between T_0 and $T_\pm$ in the ground state since these involve one electron spin flip and are degenerate. Similarly, hyperfine relaxation between X_1 and X_3/X_4 and between X_2 and X_3/X_4 should be efficient. All the data in Fig. 4(a, b) can be fit with the same values of $\Omega = 1.45 \times 2\pi$ rad/ns, $\Gamma = 2$/ns, and $\gamma_{\mathrm{hyp}} = 0.085$/ns, with only γ_{cot} changing with bias. The values of Ω and Γ can be determined from the Rabi oscillations of the RF $g^{(2)}$. The value of γ_{hyp} can most easily be determined from RF $g^{(2)}$ where it determines the optical pumping rate out of the $T_\pm$ subsystem. For weak cotunneling ($\gamma_{\mathrm{cot}} \ll \gamma_{\mathrm{hyp}}$), the bunching decay time is determined mainly by γ_{hyp}. The bunching height is determined by the combination of the γ_{cot} and γ_{hyp}, with the highest bunching when the system is most effectively pumped out of the $T_\pm$ subsystem into S. Under these conditions, the system spends most of the time in S, giving rise to a very low average count rate. However, detection of RF from the $T_\pm$ subsystem temporarily results in a much higher probability of detecting another photon until pumping returns the system to S. The values of γ_{cot} as a function of bias are obtained from fitting to the experimental data and plotted in Fig. 4(c), showing a change of almost 3 orders of magnitude. The model fits the experimental data quite well when convoluted with the temporal response of the system although there is some disagreement in the amplitude of the Rabi oscillations.

V. Two photon interference

To characterize the photon indistinguishability of Raman and RF in our QDM, we perform HOM type two-photon interference experiments using an unbalanced Mach-Zehnder interferometer, with a delay $\Delta\tau$ of 13 ns [see inset of Fig. 5(b)]. The destructive two photon interference at the second beam splitter results in the bunched photon pair exiting from one outgoing arm of the second beam splitter, resulting in a count for only one detector. This suppresses coincident events at zero time delay. $g^{HOM}(\tau)$ functions were obtained in Fig. 5(a) where two photons are linearly co-polarized [$g^{HOM}{}_{\parallel}(\tau)$] and cross-polarized [$g^{HOM}{}_{\perp}(\tau)$], respectively, enabled by rotating a half-waveplate in one arm of the interferometer. Two photons are totally distinguishable in the case of [$g^{HOM}{}_{\perp}(\tau)$]. These functions should be related to $g^{(2)}(\tau)$ by [46]

$$g^{HOM}{}_{\parallel}(\tau) = \tfrac{1}{2}g^{(2)}(\tau) + \tfrac{1}{4}\left[g^{(2)}(\tau-\Delta\tau) + g^{(2)}(\tau+\Delta\tau)\right]\left(1 - v_c e^{-2|\tau|/\tau_c}\right) \quad (1)$$

$$g^{HOM}{}_{\perp}(\tau) = \tfrac{1}{2}g^{(2)}(\tau) + \tfrac{1}{4}\left[g^{(2)}(\tau-\Delta\tau) + g^{(2)}(\tau+\Delta\tau)\right] \quad (2)$$

The mode overlap is given by v_c and should be 1 for perfect overlap, and τ_c is the coherence time of the photons. The visibility function is given by $V^{HOM}(\tau) = [g^{HOM}{}_{\perp}(\tau) - g^{HOM}{}_{\parallel}(\tau)]/g^{HOM}{}_{\perp}(\tau)$, which should go to 1 at $\tau = 0$ for $v_c = 1$ and $g^{(2)}(0) = 0$.

Fig. 5(a) shows the representative $g^{HOM}(\tau)$ result for Raman photons emitted under the condition of weak CW laser ($P = 1$ nW) resonantly driving the singlet transition at the bias of $V = 766$ mV, where the cotunneling rate is high. The coincidence count dip of co-polarized $g^{HOM}{}_{\parallel}(\tau)$ (red) nearly reaches to zero while that of cross-polarized $g^{HOM}{}_{\perp}(\tau)$ (blue) goes to 0.5 as expected from Eq. (1) and (2). The model curves in Fig. 5(a) are obtained from the previously-described model for $g^{(2)}(\tau)$ entered into Eq. (1) and (2), with $\tau_c = 1.5$ ns. Fig. 5(b) displays $V^{HOM}(\tau)$ without background subtraction or data processing. The high raw value of $V^{HOM}(0) = 0.96$ indicates strong potential for indistinguishable photons and the good mode overlap of the experiment. Based on Eqs. (1) and (2) as well as a number of recent studies, the peak value of $V^{HOM}(\tau)$ at the zero time delay under CW excitation should be always close to 1, no matter how dissimilar two photons are, provided that the instrumental response is fast compared to the coherence time of the photon [47–49]. The coherence time τ_c is likely a more meaningful value in characterizing the photons. The coherence time of $\tau_c = 1.5$ ns is nearly double the spontaneous emission time of 0.84 ns and longer than the $g^{(2)}(\tau)$ rise time of 1.1 ns. Under these low drive conditions ($\Omega/2\pi \sim 0.2$ GHz $\ll \Gamma$), one might expect an even longer τ_c for coherent Raman scatter, which can have the coherence time of the spin system for weak excitation [8,50,51]. However, under these conditions where cotunneling and the hyperfine interaction are relatively strong, the spin coherence time may be fairly short. Fluctuations in the spin splitting Δ_{exc} due to electric field fluctuations may also play a role, but this is less likely on the short time scale of the path delay $\Delta\tau$ of 13 ns.

We also examine how the HOM measurement results change for a higher laser power in Fig. 5(c) and for RF when driving the triplets in Fig. 5(d). For the higher power of 70 nW in Fig. 5(c), there is a much faster rise time for $g^{HOM}{}_{\parallel}(\tau)$ as well as for $g^{(2)}(\tau)$, shown in the inset. The change in $g^{(2)}$ rise time to 0.61 ns is explained in the previous section and is attributed to optical processes that allow the spin to reset more quickly. The value of τ_c is extracted by plugging the model for $g^{(2)}$ into Eq. 1 and adjusting τ_c to fit the measured $g^{HOM}{}_{\parallel}(\tau)$ data, giving a value of 0.35 ns. This is a much shorter coherence time than at 1 nW, which likely results from a decrease in the fraction of coherent Raman emission and perhaps other power-dependent sources of decoherence [52,53]. One might also consider whether the Raman photon wavepacket is shorter at higher powers since it is not limited by the spontaneous emission time [17].

In Fig. 5(d) the $g^{HOM}{}_{\parallel}(\tau)$ for RF and Raman under the same 1 nW drive power are very distinct. The differences are very similar to those observed in $g^{(2)}(\tau)$ (shown in the inset) and discussed in the previous section. There are damped Rabi oscillations with a fast rise time for RF and a slower rise time for Raman. The HOM dip $g^{HOM}{}_{\parallel}(0)$ is higher for RF than Raman, which is limited by the temporal resolution of our system. Despite the different behavior of $g^{(2)}(\tau)$, the coherence times obtained from fitting to Eq. 1 are not very different: 1.2 ns for RF and 1.5 ns for Raman.

VI. Conclusion

We have performed a study of the quantum optics of a driven QDM that illustrates the importance of spin. Despite the complexity of this solid state system, it can be understood and modelled quite well in an atomic picture with four ground state and four excited state energy levels. Due to the optical selection rules of different spin states, this system behaves as two partially independent subsystems, with the $S - T_0$ subsystem primarily giving Raman spin flip emission and the $T_{\pm}$ subsystem giving resonance fluorescence. The spectral properties of this driven system can be explained very well in this model even up to very high drive powers with a Rabi frequency exceeding the spin splitting. From the HBT measurements, Raman and RF have strikingly different $g^{(2)}(\tau)$ functions, which exhibit antibunching and bunching behavior, respectively, reflecting the interplay of the two subsystems and the effects of spin relaxation. From the HOM experiments, these photons are also promising for indistinguishable single photon sources. This QDM spin system is clearly quite versatile in terms of tunability and the ability to make use of different spin states for different optical processes. To select a particular optical process, the system can be initialized into a particular spin state and cavity modes can be used to enhance one transition over another. Combining this with the potentially long spin coherence times of the $S - T_0$ subsystem should enable efficient generation of highly coherent photons.

Acknowledgements

This work was supported by the US Office of Naval Research, the Defense Threat Reduction Agency (grant no. HDTRA1-15-1-0011), and the OSD Quantum Sciences and Engineering Program. S.E.E. acknowledges support from NSF under award 1839056.

Appendix: Quantum optics simulations

Quantum optics simulations of the emission spectra and $g^{(2)}(\tau)$ were performed using the Quantum Optics Toolbox in Python (QuTiP) [42,43]. The eight energy levels included in the simulation are illustrated in Fig. 1(b), along with their selection rules. Here we also give the spin configuration for each state, using an array notation in which the first (second) column represents the top (bottom) QD, and the first (second) row represents electrons (holes).

$S = \begin{pmatrix}\uparrow & \downarrow\\ 0 & 0\end{pmatrix} - \begin{pmatrix}\downarrow & \uparrow\\ 0 & 0\end{pmatrix}$	$T_0 = \begin{pmatrix}\uparrow & \downarrow\\ 0 & 0\end{pmatrix} + \begin{pmatrix}\downarrow & \uparrow\\ 0 & 0\end{pmatrix}$	$T_+ = \begin{pmatrix}\uparrow & \uparrow\\ 0 & 0\end{pmatrix}$	$T_- = \begin{pmatrix}\downarrow & \downarrow\\ 0 & 0\end{pmatrix}$
$X_1 = \begin{pmatrix}\downarrow\uparrow & \uparrow\\ \Downarrow & 0\end{pmatrix} - \begin{pmatrix}\downarrow\uparrow & \downarrow\\ \Uparrow & 0\end{pmatrix}$	$X_2 = \begin{pmatrix}\downarrow\uparrow & \uparrow\\ \Downarrow & 0\end{pmatrix} + \begin{pmatrix}\downarrow\uparrow & \downarrow\\ \Uparrow & 0\end{pmatrix}$	$X_3 = \begin{pmatrix}\downarrow\uparrow & \uparrow\\ \Uparrow & 0\end{pmatrix}$	$X_4 = \begin{pmatrix}\downarrow\uparrow & \downarrow\\ \Downarrow & 0\end{pmatrix}$

Electron spins are represented by single arrows (↑), hole spins are represented by double arrows (⇑), and a singlet spin state with two electrons in one QD is represented by ↓↑. Normalizing factors of $1/\sqrt{2}$ have been omitted. All of the exciton states are degenerate, but there is an exchange splitting Δ_{exc} between S and the triplets. X_1 and X_2 are defined as superpositions of $\begin{pmatrix}\downarrow\uparrow & \uparrow\\ \Downarrow & 0\end{pmatrix}$ and $\begin{pmatrix}\downarrow\uparrow & \downarrow\\ \Uparrow & 0\end{pmatrix}$ because these superposition states couple to linearly polarized light. Since the optical transitions are intradot, the dipole moments for the top QD with a "spectator" electron in the bottom QD are given by $\left\langle \begin{pmatrix}\downarrow\uparrow & \updownarrow\\ \Downarrow & 0\end{pmatrix} \middle| \vec{d}\cdot\hat{\sigma}_- \middle| \begin{pmatrix}\downarrow & \updownarrow\\ 0 & 0\end{pmatrix} \right\rangle = \left\langle \begin{pmatrix}\downarrow\uparrow & \updownarrow\\ \Uparrow & 0\end{pmatrix} \middle| \vec{d}\cdot\hat{\sigma}_+ \middle| \begin{pmatrix}\uparrow & \updownarrow\\ 0 & 0\end{pmatrix} \right\rangle = d_0$. Applying this to the 8 level system gives the polarization selection rules in Fig. 1(b), where the dipole moments of the linearly polarized

transitions of the double-Λ subsystem are reduced by $1/\sqrt{2}$ with respect to the circularly polarized $T_\pm$ transitions. However, the Rabi frequencies Ω when driving the system with linearly polarized light are identical for all transitions since the circularly polarized $T_\pm$ transitions are reduced by $\hat{\sigma}_\pm \cdot \hat{x} = 1/\sqrt{2}$. We also note that the choice of linear polarization basis is arbitrary. There is no difference in the appearance of the selection rules for any linear polarization basis, except that the definitions of X_1 and X_2 will change.

The Hamiltonian of the driven system in the rotating frame of the laser field, with the rotating wave approximation, is given by

$$H = \delta_S|S\rangle\langle S| + \delta_T|T_0\rangle\langle T_0| + \delta_T|T_+\rangle\langle T_+| + \delta_T|T_-\rangle\langle T_-| \\ +\frac{1}{2}\Omega\sigma_{S,X_1} + \frac{1}{2}\Omega\sigma_{T_0,X_2} + \frac{1}{2}\Omega\sigma_{T_+,X_3} + \frac{1}{2}\Omega\sigma_{T_-,X_4} + \text{h.c.} \quad (1)$$

where δ_S and δ_T are the detuning of the laser from the singlet and triplet transitions, respectively, $\sigma_{A,B} = |A\rangle\langle B|$, and "h.c." is the Hermitian conjugates of the off-diagonal terms. Decay and decoherence are included by collapse operators. These include collapse operators representing spontaneous emission C^i_{rad}, pure optical dephasing C^i_{phas}, spin relaxation from cotunneling C^i_{cot}, and spin relaxation from the hyperfine interaction C^i_{hyp}. The collapse operators for spontaneous emission are given below:

$$C^i_{\text{rad}}: \sqrt{\tfrac{1}{2}\Gamma}\sigma_{S,X_1}, \sqrt{\tfrac{1}{2}\Gamma}\sigma_{S,X_2}, \sqrt{\tfrac{1}{2}\Gamma}\sigma_{T_0,X_1}, \sqrt{\tfrac{1}{2}\Gamma}\sigma_{T_0,X_2}, \sqrt{\Gamma}\sigma_{T_+,X_3}, \sqrt{\Gamma}\sigma_{T_-,X_4} \quad (2)$$

As discussed previously, the dipole moments (and decay operators) for the linearly polarized $S - T_0$ transitions are weaker by $1/\sqrt{2}$. Since there are two decay channels for X_1 and X_2, the overall lifetime of these states is the same as X_3 and X_4. Pure optical dephasing collapse operators C^i_{phas} are also included for all allowed optical transitions, for example $C^1_{\text{phas}} = \sqrt{\Gamma}(|S\rangle\langle S| - |X_1\rangle\langle X_1|)$.

Spin relaxation from cotunneling is included equally between all spin states in the ground state and excited state, with collapse operators such as $C^1_{\text{cot}} = \sqrt{\gamma_{\text{cot}}}\sigma_{S,T_0}$ and $C^2_{\text{cot}} = \sqrt{\gamma_{\text{cot}}}\sigma_{T_0,S}$. The two relaxation rates are approximated as equal since $k_BT > \Delta_{\text{exc}}$. Spin relaxation due to the hyperfine interaction is included between T_0 and $T_\pm$: $C^1_{\text{hyp}} = \sqrt{\gamma_{\text{hyp}}}\sigma_{T_0,T_-}$, $C^3_{\text{hyp}} = \sqrt{\gamma_{\text{hyp}}}\sigma_{T_0,T_+}$, and h.c. of each. Hyperfine coupling is efficient between these states because they change M_s by ±1 and are degenerate. For the same reasons, the hyperfine interaction couples X_1 and X_2 to X_3 and X_4: $C^5_{\text{hyp}} = \sqrt{\frac{1}{2}\gamma_{\text{hyp}}}\sigma_{X_1,X_3}$, $C^7_{\text{hyp}} = \sqrt{\frac{1}{2}\gamma_{\text{hyp}}}\sigma_{X_1,X_4}$, $C^9_{\text{hyp}} = \sqrt{\frac{1}{2}\gamma_{\text{hyp}}}\sigma_{X_2,X_3}$, $C^{11}_{\text{hyp}} = \sqrt{\frac{1}{2}\gamma_{\text{hyp}}}\sigma_{X_2,X_4}$, and h.c. of each. These coupling are weaker by $1/\sqrt{2}$ since only one of the two components of X_1 or X_2 couples to X_3 or X_4. The hyperfine interaction with hole spins is neglected. This model for relaxation may be simplistic and not include all possible processes. For instance, valence band mixing may allow nominally forbidden transitions to occur, but this should give essentially the same effect as a spin flip in the exciton state. This model captures the essential physics and reproduces the experimental data well. One important aspect is that the relaxation between $T_\pm$ and T_0 must be significantly faster than between S and the triplets in order to obtain the large bunching in RF observed in Fig. 4(b). This difference in rates allows efficient pumping out of the $T_\pm$ states.

Correlation functions $G^{(1)}(\tau) = \langle \sigma^\dagger(t)\sigma(t+\tau)\rangle$ and $G^{(2)}(\tau) = \langle \sigma^\dagger(t)\sigma^\dagger(t+\tau)\sigma(t+\tau)\sigma(t)\rangle$ are calculated in QuTiP using the quantum regression theorem [54]. There are four allowed emission transitions, with associated operators σ_{S,X_2}, σ_{T_0,X_1}, σ_{T_+,X_3}, and σ_{T_-,X_4}, and correlation functions are calculated for each. Using the quantum regression theorem, $G^{(1)}_{S,X_2}(\tau)$ can be evaluated by the time evolution of an operator Λ with the master equation, starting from the initial condition $\Lambda(0) = \rho(t \to \infty)\sigma^\dagger_{S,X_2}$, where $\rho(t \to \infty)$ is the steady state density matrix. Then, $G^{(1)}_{S,X_2}(\tau) = \mathrm{Tr}\left[\sigma_{S,X_2}\Lambda(\tau)\right]$, and the emission spectrum $S_{S,X_2}(\omega)$ can be calculated with the Fourier transform of $G^{(1)}_{S,X_2}(\tau)$, taking into account the frequency offset from the rotating frame. $G^{(2)}_{S,X_2}(\tau)$ can be evaluated in a similar manner with $\Lambda(0) = \sigma_{S,X_2}\rho(t \to \infty)\sigma^\dagger_{S,X_2}$ and $G^{(2)}_{S,X_2}(\tau) = \mathrm{Tr}\left[\sigma^\dagger_{S,X_2}\sigma_{S,X_2}\Lambda(\tau)\right]$. This simplifies to finding $\Lambda_{X_2,X_2}(\tau)$ starting from $\Lambda(0) = |S\rangle\langle S|$. These functions can be normalized by dividing by their values at $\tau \to \infty$.

To obtain the full emission spectrum, the spectral functions of all four operators are summed. For $g^{(2)}(\tau)$ measurements where only one spectral feature is measured, only a particular correlation function is used. For Raman $g^{(2)}(\tau)$ when driving the triplets, $G^{(2)}_{S,X_2}(\tau)$ is used. For Raman $g^{(2)}(\tau)$ when driving the singlet, $G^{(2)}_{T_0,X_1}(\tau)$ is used. For RF $g^{(2)}(\tau)$ when driving the triplets, either $G^{(2)}_{T_+,X_3}(\tau)$ or $G^{(2)}_{T_-,X_4}(\tau)$ is used, but these functions are modified slightly to account for the fact that emission from either transition will be detected: $G^{(2)}_{T_-,X_4}(\tau) = \Lambda_{X_3,X_3}(\tau) + \Lambda_{X_4,X_4}(\tau)$, with $\Lambda(0) = |T_-\rangle\langle T_-|$.

[1] S. Buckley, K. Rivoire, and J. Vučković, Engineered quantum dot single-photon sources., Rep. Prog. Phys. **75**, 126503 (2012).

[2] O. Gazzano and G. S. Solomon, Toward optical quantum information processing with quantum dots coupled to microstructures, J. Opt. Soc. Am. B **33**, C160 (2016).

[3] P. Michler, A. Kiraz, C. Becher, W. V Schoenfeld, P. M. Petroff, L. Zhang, E. Hu, and A. Imamoglu, A Quantum Dot Single-Photon Turnstile Device, Science **290**, 2282 (2000).

[4] C. Santori, M. Pelton, G. Solomon, Y. Dale, and Y. Yamamoto, Triggered single photons from a quantum dot, Phys. Rev. Lett. **86**, 1502 (2001).

[5] N. Somaschi, V. Giesz, L. De Santis, J. C. Loredo, M. P. Almeida, G. Hornecker, S. L. Portalupi, T. Grange, C. Antón, J. Demory, C. Gómez, I. Sagnes, N. D. Lanzillotti-Kimura, A. Lemaítre, A. Auffeves, A. G. White, L. Lanco, and P. Senellart, Near-optimal single-photon sources in the solid state, Nat. Photonics **10**, 340 (2016).

[6] C. Santori, D. Fattal, J. Vucković, G. S. Solomon, and Y. Yamamoto, Indistinguishable photons from a single-photon device., Nature **419**, 594 (2002).

[7] Y.-M. He, Y. He, Y.-J. Wei, D. Wu, M. Atatüre, C. Schneider, S. Höfling, M. Kamp, C.-Y. Lu, and J.-W. Pan, On-demand semiconductor single-photon source with near-unity indistinguishability., Nat. Nanotechnol. **8**, 213 (2013).

[8] Y. He, Y.-M. He, Y.-J. Wei, X. Jiang, M.-C. Chen, F.-L. Xiong, Y. Zhao, C. Schneider, M. Kamp, S. Höfling, C.-Y. Lu, and J.-W. Pan, Indistinguishable Tunable Single Photons Emitted by Spin-Flip Raman Transitions in InGaAs Quantum Dots, Phys. Rev. Lett. **111**, 237403 (2013).

[9] E. B. Flagg, A. Muller, J. W. Robertson, S. Founta, D. G. Deppe, M. Xiao, W. Ma, G. J. Salamo, and C. K. Shih, Resonantly driven coherent oscillations in a solid-state quantum emitter, Nat. Phys. **5**, 203 (2009).

[10] A. N. Vamivakas, Y. Zhao, C.-Y. Lu, and M. Atatüre, Spin-resolved quantum-dot resonance

fluorescence, Nat. Phys. **5**, 198 (2009).
[11] S. Ates, S. M. Ulrich, S. Reitzenstein, A. Löffler, A. Forchel, and P. Michler, Post-Selected Indistinguishable Photons from the Resonance Fluorescence of a Single Quantum Dot in a Microcavity, Phys. Rev. Lett. **103**, 167402 (2009).
[12] X. Xu, B. Sun, P. R. Berman, D. G. Steel, A. S. Bracker, D. Gammon, and L. J. Sham, Coherent Optical Spectroscopy of a Strongly Driven Quantum Dot, Science **317**, 929 (2007).
[13] X. Xu, Y. Wu, B. Sun, Q. Huang, J. Cheng, D. G. Steel, a. S. Bracker, D. Gammon, C. Emary, and L. J. Sham, Fast Spin State Initialization in a Singly Charged InAs-GaAs Quantum Dot by Optical Cooling, Phys. Rev. Lett. **99**, 097401 (2007).
[14] M. Atatüre, J. Dreiser, A. Badolato, A. Högele, K. Karrai, and A. Imamoglu, Quantum-dot spin-state preparation with near-unity fidelity., Science **312**, 551 (2006).
[15] G. Fernandez, T. Volz, R. Desbuquois, A. Badolato, and A. Imamoglu, Optically Tunable Spontaneous Raman Fluorescence from a Single Self-Assembled InGaAs Quantum Dot, Phys. Rev. Lett. **103**, 087406 (2009).
[16] T. M. Sweeney, S. G. Carter, A. S. Bracker, M. Kim, C. S. Kim, L. Yang, P. M. Vora, P. G. Brereton, E. R. Cleveland, and D. Gammon, Cavity-stimulated Raman emission from a single quantum dot spin, Nat. Photonics **8**, 442 (2014).
[17] B. C. Pursley, S. G. Carter, M. K. Yakes, A. S. Bracker, and D. Gammon, Picosecond pulse shaping of single photons using quantum dots, Nat. Commun. **9**, 115 (2018).
[18] L. Béguin, J. P. Jahn, J. Wolters, M. Reindl, Y. Huo, R. Trotta, A. Rastelli, F. Ding, O. G. Schmidt, P. Treutlein, and R. J. Warburton, On-demand semiconductor source of 780-nm single photons with controlled temporal wave packets, Phys. Rev. B **97**, 205304 (2018).
[19] W. B. Gao, P. Fallahi, E. Togan, and A. Imamoglu, Observation of entanglement between a quantum dot spin and a single photon, Nature **491**, 426 (2012).
[20] K. De Greve, L. Yu, P. L. Mcmahon, J. S. Pelc, C. M. Natarajan, N. Y. Kim, E. Abe, S. Maier, C. Schneider, M. Kamp, S. Hofling, R. H. Hadfield, A. Forchel, and M. M. Fejer, Quantum-dot spin-photon entanglement via frequency downconversion to telecom wavelength, Nature **491**, 421 (2012).
[21] J. R. Schaibley, a. P. Burgers, G. a. McCracken, L.-M. Duan, P. R. Berman, D. G. Steel, a. S. Bracker, D. Gammon, and L. J. Sham, Demonstration of Quantum Entanglement between a Single Electron Spin Confined to an InAs Quantum Dot and a Photon, Phys. Rev. Lett. **110**, 167401 (2013).
[22] S. G. Carter, T. M. Sweeney, M. Kim, C. S. Kim, D. Solenov, S. E. Economou, T. L. Reinecke, L. Yang, A. S. Bracker, and D. Gammon, Quantum Control of a Spin Qubit Coupled to a Photonic Crystal Cavity, Nat. Photonics **7**, 329 (2013).
[23] A. Delteil, Z. Sun, W. Gao, E. Togan, S. Faelt, and A. Imamoğlu, Generation of heralded entanglement between distant hole spins, Nat. Phys. **12**, 218 (2016).
[24] Y. L. Delley, M. Kroner, S. Fält, W. Wegscheider, and A. İmamoğlu, Deterministic entanglement between a propagating photon and a singlet--triplet qubit in an optically active quantum dot molecule, Phys. Rev. B **96**, 241410(R) (2017).
[25] E. A. Stinaff, M. Scheibner, A. S. Bracker, I. V Ponomarev, V. L. Korenev, M. E. Ware, M. F. Doty, T. L. Reinecke, and D. Gammon, Optical signatures of coupled quantum dots, Science **311**, 636 (2006).
[26] H. Krenner, E. Clark, T. Nakaoka, M. Bichler, C. Scheurer, G. Abstreiter, and J. Finley, Optically Probing Spin and Charge Interactions in a Tunable Artificial Molecule, Phys. Rev. Lett. **97**, 076403 (2006).
[27] M. Doty, M. Scheibner, A. Bracker, I. Ponomarev, T. Reinecke, and D. Gammon, Optical spectra of doubly charged quantum dot molecules in electric and magnetic fields, Phys. Rev. B **78**, 115316 (2008).

[28] D. Kim, S. G. Carter, A. Greilich, A. S. Bracker, and D. Gammon, Ultrafast optical control of entanglement between two quantum-dot spins, Nat. Phys. **7**, 223 (2011).
[29] K. M. Weiss, J. M. Elzerman, Y. L. Delley, J. Miguel-Sanchez, and A. Imamoğlu, Coherent Two-Electron Spin Qubits in an Optically Active Pair of Coupled InGaAs Quantum Dots, Phys. Rev. Lett. **109**, 107401 (2012).
[30] C. M. Chow, A. M. Ross, D. Kim, D. Gammon, A. S. Bracker, L. J. Sham, and D. G. Steel, Nonlocal Nuclear Spin Quieting in Quantum Dot Molecules: Optically Induced Extended Two-Electron Spin Coherence Time, Phys. Rev. Lett. **117**, 077403 (2016).
[31] J. M. Elzerman, K. M. Weiss, J. Miguel-Sanchez, and A. Imamo□lu, Optical Amplification Using Raman Transitions between Spin-Singlet and Spin-Triplet States of a Pair of Coupled In-GaAs Quantum Dots, Phys. Rev. Lett. **107**, 017401 (2011).
[32] P. M. Vora, A. S. Bracker, S. G. Carter, T. M. Sweeney, M. Kim, C. S. Kim, L. Yang, P. G. Brereton, S. E. Economou, and D. Gammon, Spin–cavity interactions between a quantum dot molecule and a photonic crystal cavity, Nat. Commun. **6**, 7665 (2015).
[33] R. H. Brown and R. Q. Twiss, Correlation between photons in two coherent beams of light, Nature **177**, 27 (1956).
[34] C. K. Hong, Z. Y. Ou, and L. Mandel, Measurement of Subpicosecond Time Intervals between Two Photons by Interference, Phys. Rev. Lett. **59**, 2044 (1987).
[35] A. Muller, E. B. Flagg, P. Bianucci, X. Y. Wang, D. G. Deppe, W. Ma, J. Zhang, G. J. Salamo, M. Xiao, and C. K. Shih, Resonance Fluorescence from a Coherently Driven Semiconductor Quantum Dot in a Cavity, Phys. Rev. Lett. **99**, 187402 (2007).
[36] C. Cohen-Tannoudji and S. Reynaud, Modification of resonance Raman scattering in very intense laser fields, J. Phys. B At. Mol. Phys. **10**, 365 (1977).
[37] J. M. Smith, P. A. Dalgarno, R. J. Warburton, A. O. Govorov, K. Karrai, B. D. Gerardot, and P. M. Petroff, Voltage control of the spin dynamics of an exciton in a semiconductor quantum dot, Phys. Rev. Lett. **94**, 197402 (2005).
[38] J. Dreiser, M. Atatüre, C. Galland, T. Müller, A. Badolato, and A. Imamoglu, Optical investigations of quantum dot spin dynamics as a function of external electric and magnetic fields, Phys. Rev. B **77**, 075317 (2008).
[39] B. Alén, F. Bickel, K. Karrai, R. J. Warburton, and P. M. Petroff, Stark-shift modulation absorption spectroscopy of single quantum dots, Appl. Phys. Lett. **83**, 2235 (2003).
[40] S. H. Autler and C. H. Townes, Stark Effect in Rapidly Varying Fields, Phys. Rev. **100**, 703 (1955).
[41] B. R. Mollow, Power spectrum of light scattered by two-level systems, Phys. Rev. **188**, 1969 (1969).
[42] J. R. Johansson, P. D. Nation, and F. Nori, QuTiP: An open-source Python framework for the dynamics of open quantum systems, Comput. Phys. Commun. **183**, 1760 (2012).
[43] J. R. Johansson, P. D. Nation, and F. Nori, QuTiP 2: A Python framework for the dynamics of open quantum systems, Comput. Phys. Commun. **184**, 1234 (2013).
[44] C. Santori, Generation of nonclassical light using semiconductor quantum dots (Doctoral dissertation, Stanford university, 2003).
[45] S. T. Yılmaz, P. Fallahi, and A. Imamoğlu, Quantum-Dot-Spin Single-Photon Interface, Phys. Rev. Lett. **105**, 033601 (2010).
[46] R. B. Patel, A. J. Bennett, K. Cooper, P. Atkinson, C. A. Nicoll, D. A. Ritchie, and A. J. Shields, Postselective two-photon interference from a continuous nonclassical stream of photons emitted by a quantum dot, Phys. Rev. Lett. **100**, 207405 (2008).
[47] R. Proux, M. Maragkou, E. Baudin, C. Voisin, P. Roussignol, and C. Diederichs, Measuring the Photon Coalescence Time Window in the Continuous-Wave Regime for Resonantly Driven Semiconductor Quantum Dots, Phys. Rev. Lett. **114**, 067401 (2015).

[48] T. Legero, T. Wilk, A. Kuhn, and G. Rempe, Time-resolved two-photon quantum interference, Appl. Phys. B Lasers Opt. **77**, 797 (2003).
[49] B. Kambs and C. Becher, Limitations on the indistinguishability of photons from remote solid state sources, New J. Phys. **20**, 115003 (2018).
[50] C. Santori, D. Fattal, K.-M. C. Fu, P. E. Barclay, and R. G. Beausoleil, On the indistinguishability of Raman photons, New J. Phys. **11**, 123009 (2009).
[51] Z. Sun, A. Delteil, S. Faelt, and A. Imamoglu, Measurement of spin coherence using Raman scattering, Phys. Rev. B **93**, 241302(R) (2016).
[52] A. J. Bennett, D. C. Unitt, A. J. Shields, P. Atkinson, and D. A. Ritchie, Influence of exciton dynamics on the interference of two photons from a microcavity single-photon source, Opt. Express **13**, 7772 (2005).
[53] L. Monniello, C. Tonin, R. Hostein, A. Lemaitre, A. Martinez, V. Voliotis, and R. Grousson, Excitation-Induced Dephasing in a Resonantly Driven InAs/GaAs Quantum Dot, Phys. Rev. Lett. **111**, 026403 (2013).
[54] D. A. Steck, Quantum and Atom Optics, *Quantum and Atom Optics* (2007).

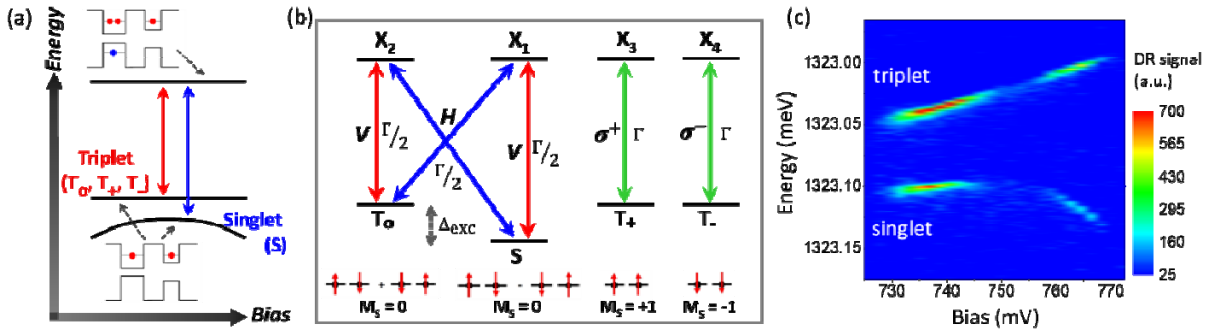

FIG. 1 (a) Schematic diagram for the bias dependent energy levels for the ground and excited states of the QDM charged with one electron in each dot. The ground state of the spin singlet ( ) is energetically separated from the triplets (,) due to the exchange splitting. (b) Detailed energy level diagram of the two-electron charged QDM with the ground state spin structure and the optical selection rules. H and V: horizontal and vertical polarization; and : left- and right-circular polarization; : relaxation rate. (c) Measured contour bias map of differential reflectance spectra.

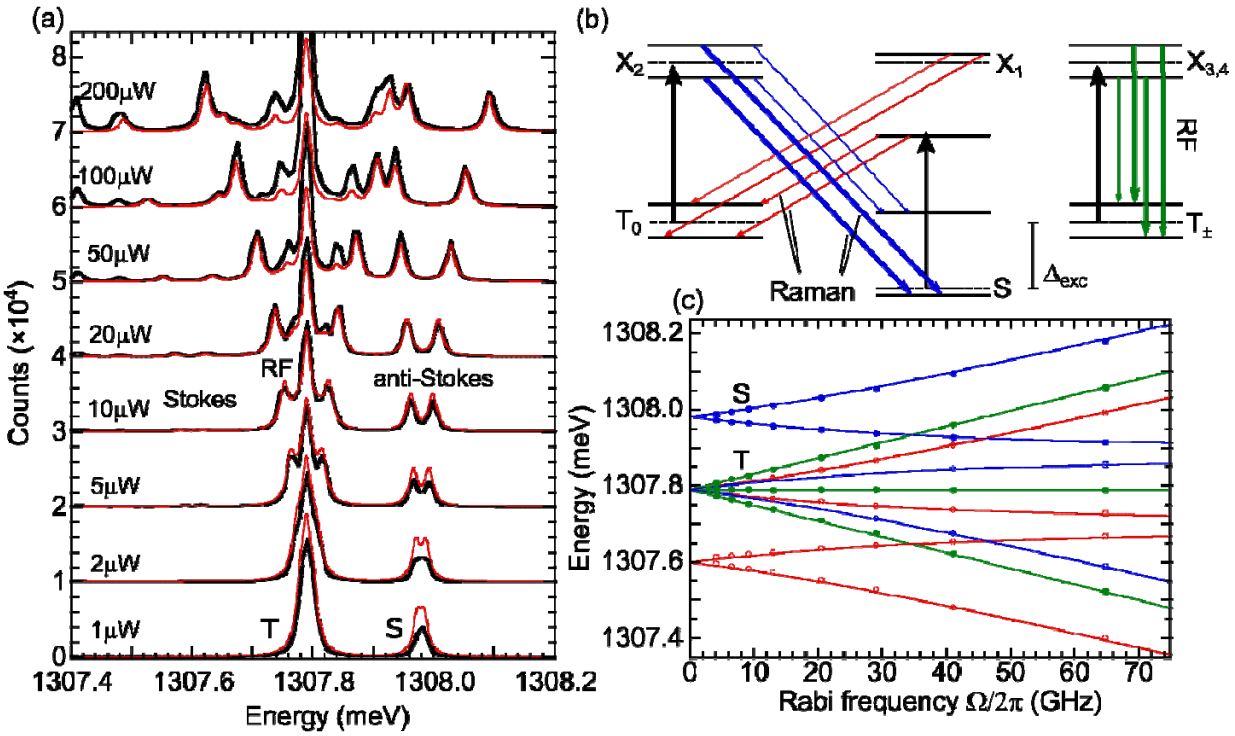

FIG. 2 (a) Experimental (black) and simulated (red) emission spectra when driving the triplet transitions for a series of drive powers. (b) Dressed state energy level diagram when resonantly driving the triplet transitions. Solid horizontal lines are dressed states, and dashed horizontal lines are the bare energy levels. Vertical black arrows represent the vertically polarized laser, and diagonal arrows between dressed states represent horizontally polarized emission. (c) Measured peak positions (circles) and modelled dressed state transitions (lines) as a function of Rabi frequency, with colors corresponding to the transitions shown in (b).

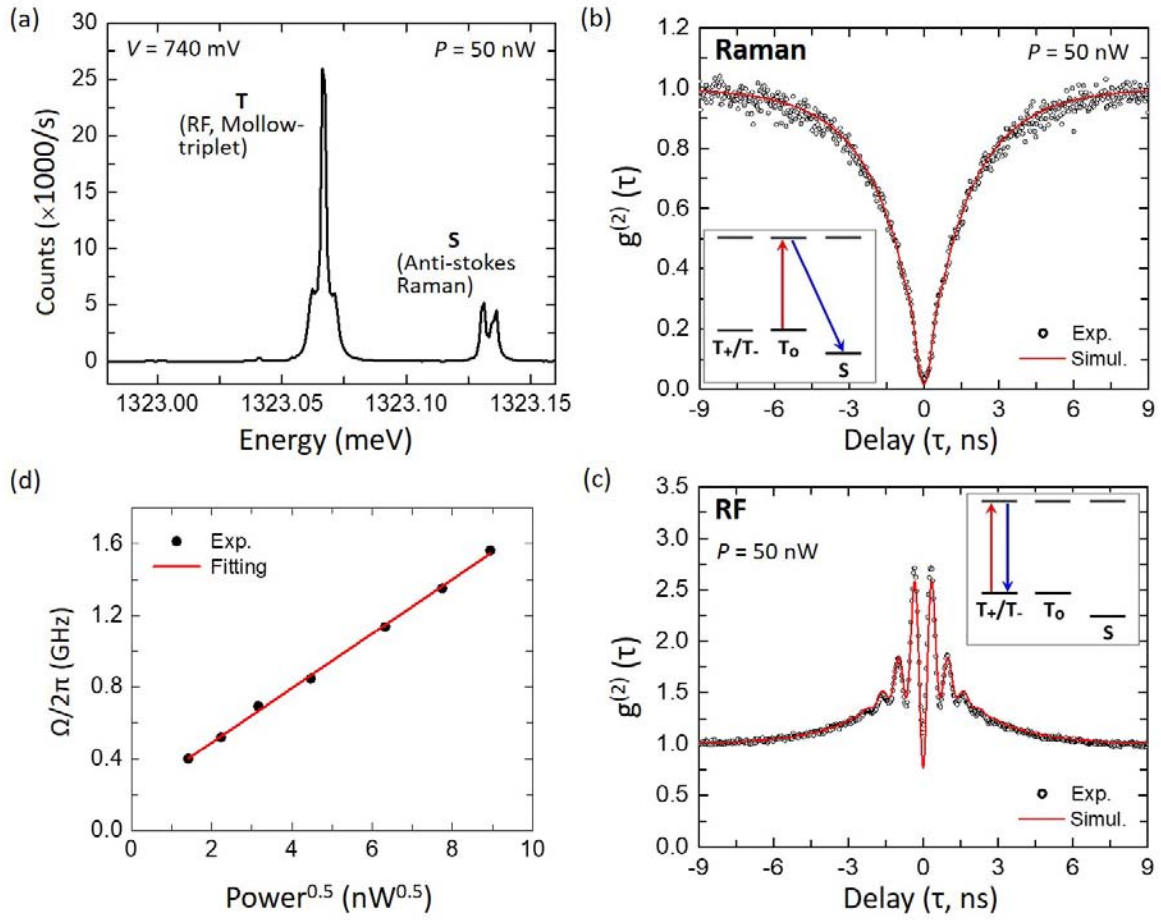

FIG. 3 (a) High-resolution emission spectrum from the laser resonantly driving the triplet transition. The Mollow triplet (RF) and Autler-Townes doublet (Raman) are observed at the energies of the triplets (T) and singlet (S), respectively. (b),(c) Measured second order correlation function (black open dots) with a simulated curve (red line) for Raman and RF emissions in (b) and (c), respectively. Insets display the excitation and emission processes. (d) Relation between the measured Rabi frequency and the laser drive power extracted from the $g^{(2)}$ functions for RF. Rabi frequencies scale with the square root of the drive power.

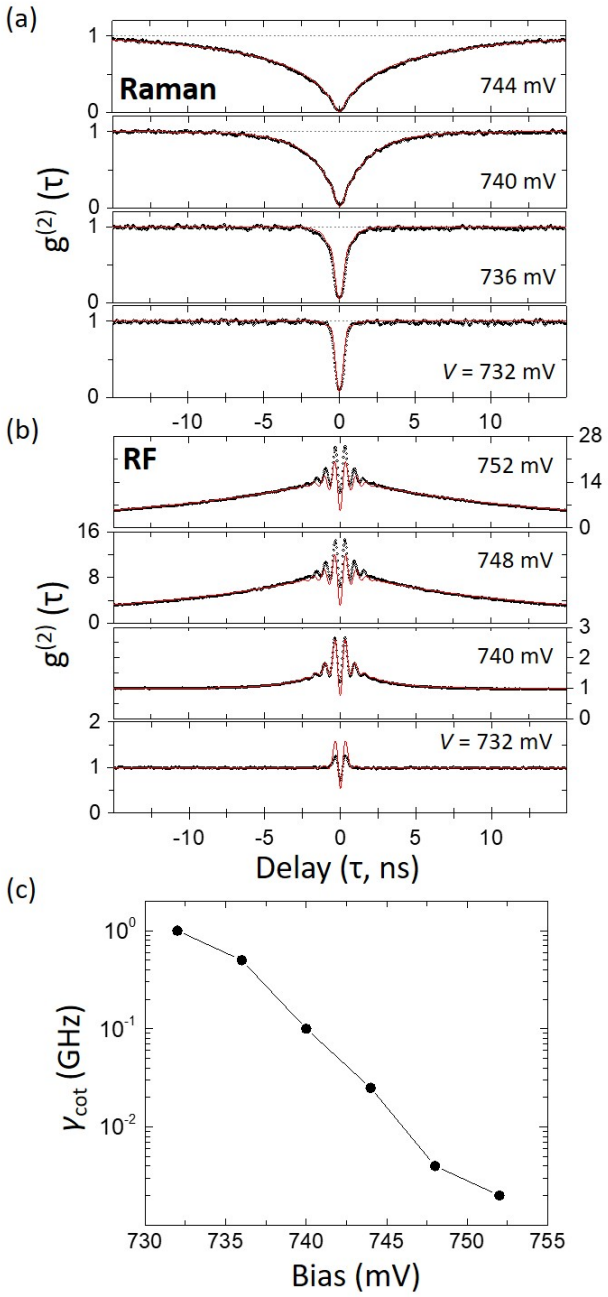

FIG. 4 (a),(b) Bias-dependent $g^{(2)}$ functions (black dots) for Raman and RF at several different biases, with simulated functions in red. All measured $g^{(2)}$ functions are normalized with the average coincidence count at a delay τ far from bunching or anti-bunching features. (c) Cotunneling relaxation rate (γ_{cot}) obtained from simulations of the experimental data as a function of the applied bias.

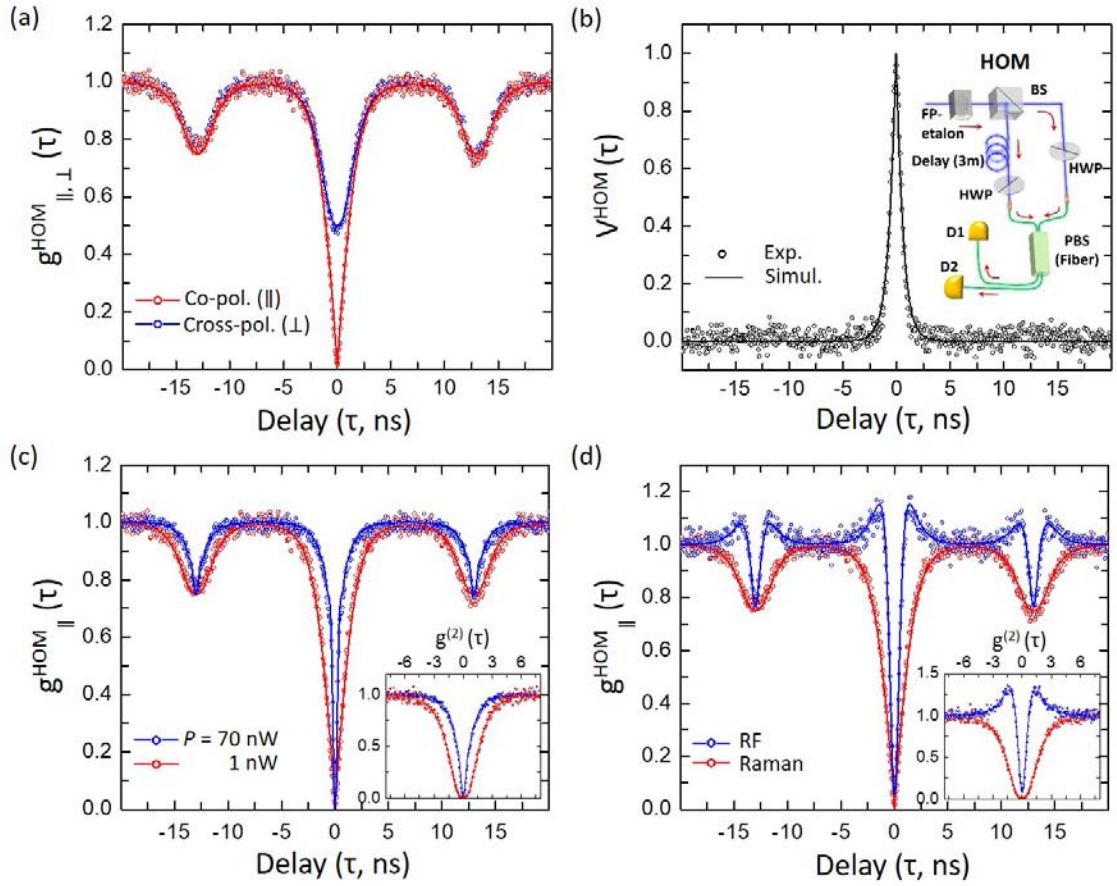

FIG. 5 (a) HOM-type two-photon interference experiments for Raman emission with linearly co-(∥, red) and cross-polarized (⊥, blue) photons measured with an unbalanced Mach-Zehnder interferometer. (b) HOM visibility function derived from co- and cross-polarized $g^{HOM}{}_{\parallel}(\tau)$ and $g^{HOM}{}_{\perp}(\tau)$ plotted in (a). Inset shows our experimental setup. (c) Power-dependent co-polarized $g^{HOM}{}_{\parallel}(\tau)$ for Raman with two different laser excitation powers. (d) Comparison of $g^{HOM}{}_{\parallel}(\tau)$ between Raman and RF under the same experimental conditions. Insets in (c), (d) are the corresponding second-order correlation functions. Open circles display the measured coincidence counts while lines represent the QuTiP simulations.